Nano-Micro Letters

e-ISSN 2150-5551
CN 31-2103/TB

ARTICLE

https://doi.org/10.1007/s40820-025-01788-z

Cite as
Nano-Micro Lett.
(2025) 17:310

Received: 12 February 2025
Accepted: 24 April 2025

Face-/Edge-Shared 3D Perovskitoid Single Crystals with Suppressed Ion Migration for Stable X-Ray Detector

Zimin Zhang[1], Xiaoli Wang[2,3], Huayang Li[1] ✉, Dong Li[2], Yang Zhang[2], Nan Shen[1], Xue-Feng Yu[2,3,4], Yucheng Liu[5], Shengzhong Liu[5,6], Haomin Song[7], Yanliang Liu[2,3,4] ✉, Xingzhu Wang[8] ✉, Shi Chen[1] ✉

HIGHLIGHTS

- 3D perovskitoid $Pb_2CuGly_2X_4$ (Gly = -O_2C-CH_2-NH_2; X = Cl, Br) single crystals (SCs) with face-/edge-shared inorganic skeleton and $CuGly_2$ pillars delivered a high ion migration activation energy of 1.06 eV.
- The $Pb_2CuGly_2Cl_4$ SC X-ray detector presented low dark current drift (1.20×10^{-9} nA mm^{-1} s^{-1} V^{-1} at 120 V mm^{-1}) and high sensitivity (9250 μC Gy^{-1} cm^{-2}).
- The $Pb_2CuGly_2Cl_4$ film-based thin-film transistor array detector offered an X-ray imaging capability with spatial resolution of 2.2 lp mm^{-1}.

ABSTRACT Although three-dimensional metal halide perovskites are promising candidates for direct X-ray detection, the ion migration of perovskites seriously affects the detector stability. Herein, face-/edge-shared 3D heterometallic glycinate hybrid perovskitoid $Pb_2CuGly_2X_4$ (Gly = -O_2C-CH_2-NH_2; X = Cl, Br) single crystals (SCs), in which the adjacent lead halide layers are linked by large-sized $Cu(Gly)_2$ pillars, are synthesized in water. The $Cu(Gly)_2$ pillars in combination with face-/edge-shared inorganic skeleton are found able to synergistically suppress the ion migration, delivering a high ion migration activation energy (E_a) of 1.06 eV. The $Pb_2CuGly_2Cl_4$ SC X-ray detector displays extremely low dark current drift of 1.20×10^{-9} nA mm^{-1} s^{-1} V^{-1} under high electric field (120 V mm^{-1}) and continuous X-ray irradiation (2.86 Gy), and a high sensitivity of 9,250 μC Gy^{-1} cm^{-2} is also achieved. More excitingly, the $Pb_2CuGly_2Cl_4$ nanocrystal can be easily dispersed in water and directly blade-coated on thin-film transistor (TFT) array substrate, and the obtained $Pb_2CuGly_2Cl_4$-based TFT array detector offers an X-ray imaging capability with spatial resolution of 2.2 lp mm^{-1}.

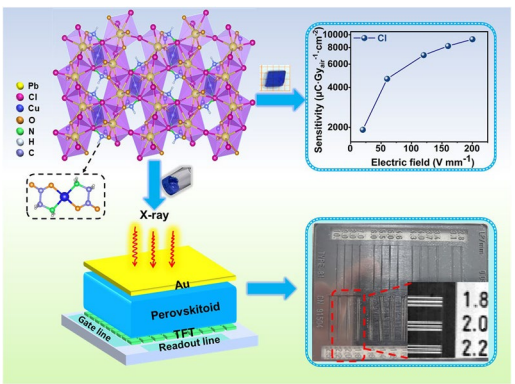

KEYWORDS 3D perovskitoid; Single crystals; Suppressed ion migration; High operating stability; X-ray detector

Zimin Zhang and Xiaoli Wang contributed equally to this work.
✉ Huayang Li, lhychem@henu.edu.cn; Yanliang Liu, yl.liu4@siat.ac.cn; Xingzhu Wang, wangxz@sustech.edu.cn; Shi Chen, chenshi@henu.edu.cn
[1] Henan Key Laboratory of Quantum Materials and Quantum Energy, School of Future Technology, Henan University, Zhengzhou 450046, People's Republic of China
[2] Shenzhen Institute of Advanced Technology, Chinese Academy of Sciences, Shenzhen, Guangdong 518055, People's Republic of China
[3] University of Chinese Academy of Sciences, Beijing 100049, People's Republic of China
[4] Key Laboratory of Biomedical Imaging Science and System, Chinese Academy of Sciences, Shenzhen, Guangdong 518055, People's Republic of China
[5] Key Laboratory of Applied Surface and Colloid Chemistry, Shaanxi Engineering Lab for Advanced Energy Technology, School of Materials Science and Engineering, National Ministry of Education, Shaanxi Normal University, Xi'an 710119, People's Republic of China
[6] State Key Laboratory of Catalysis, Dalian National Laboratory for Clean Energy, Dalian Institute of Chemical Physics, Chinese Academy of Sciences, Dalian 116023, People's Republic of China
[7] Institute of Applied Physics and Materials Engineering, University of Macau, Taipa, Macau, SAR 999078, People's Republic of China
[8] School of Electrical Engineering, University of South China, Hengyang 421001, People's Republic of China

Published online: 23 June 2025

1 Introduction

X-ray detection, as an efficient nondestructive technique, has been widely applied in various fields such as industrial inspection, medical diagnosis, security checks and homeland defense [1]. The lead halide perovskites, as emerging but efficient photovoltaic materials, have more potential in assembling next-generation cost-effective and highly sensitive X-ray detector due to their high X-ray attenuation coefficient, high defect tolerance, large carrier mobility–lifetime product ($\mu\tau$), diverse dimensions and facile preparation process as well as inexpensive raw materials. Three-dimensional (3D) perovskite single crystals (SCs) including methylammonium lead bromide ($MAPbBr_3$), methylammonium lead iodide ($MAPbI_3$), cesium lead bromide ($CsPbBr_3$) and formamidine lead iodide ($FAPbI_3$) have been successfully synthesized to manufacture SC-based X-ray detectors [2–8], and for instance, the high sensitivity of 3D perovskite SC-based X-ray detector has been realized, displaying more than three orders of magnitude higher than that of commercial α-Se-based detector [9, 10]. However, the conventional 3D perovskite SCs are ionic compounds, and they are prone to ion migration under applied electric field [11]. This phenomenon will cause the baseline drift so as to the instability of response signals, which largely hampers the long-term operating stability of detectors, thereby limiting their commercial application [12].

Based on this situation, various strategies including device architecture optimization [10, 13], regulation of the quality of perovskite SCs [6, 8, 11, 14], interface passivation [7] and heterojunction design [9, 15, 16] have been proposed to inhibit the ion migration in perovskites, but the derived dark current drift of 3D perovskite SCs under large electric field still remains a daunting challenge. Therefore, the crystal structure design of perovskite materials is a fundamental method to sufficiently suppress intrinsic ion migration and construct stable X-ray detector.

One latest research work demonstrated that the inorganic networks in perovskites with edge- and face-sharing mode were more robust than that with corner-sharing mode, which is able to effectively impede the ion migration [17]. Besides, the large-sized organic cations in perovskites were also found able to efficiently block the ion migration [18–20]. For example, Zhang et al. introduced DGA (dimethylbiguanide) as an organic cation and fabricated the 2D perovskite SC $(DGA)PbI_4$. The $(DGA)PbI_4$ SC detector displayed a negligible dark current drift under an electric field of 200 V mm^{-1} for 5,426 s due to the suppressed ion migration [19]. However, this category of perovskite crystal structures combining edge-/face-sharing skeleton with large-sized cations is almost discovered in low-dimensional perovskites [21, 22]. Considering the low detection sensitivity of low-dimensional perovskites induced by the limited charge transport, constructing 3D perovskites with both edge-/face-sharing skeleton and large-sized cations to fully suppress the ion migration without sacrificing the sensitivity is highly imperative.

Since large-sized zwitterionic amino acids ligands have electron-rich amine and carboxylate groups, they can not only coordinate with the metal ion to form robust organic metal cross-linked cluster as a large-sized spacer [23–25], but also form strong bonding with lead halide polyhedrons and result in the formation of edge-/face-sharing skeleton [26], basically satisfying the above-mentioned structure design rule of 3D perovskites. Based on this idea, the 3D perovskitoid SC $Pb_2CuGly_2Br_4$ ($Gly = -O_2C\text{-}CH_2\text{-}NH_2$) was developed and reported to be a promising material for X-ray detection [27, 29]. However, the photoelectric properties of halide-modulated $Pb_2CuGly_2X_4$ (X = Cl, Br) SCs and their final X-ray detection performance have not yet been systematically explored. Given these considerations, herein, we synthesized high-quality 3D heterometallic glycinate hybrid perovskitoid $Pb_2CuGly_2X_4$ (X = Cl, Br) SCs via water evaporation method. The lead halide layers are linked by the robust $Cu(Gly)_2$ units via the Pb–O bonds, leading to the formation of 3D framework. The $Cu(Gly)_2$ pillars and robust inorganic networks enabled by face-/edge-shared $[PbX_5O_3]^{9-}$ dodecahedron synergistically are able to effectively inhibit the ion migration, resulting in a high ion activation energy (E_a). The $Pb_2CuGly_2Cl_4$ SC exhibits lower microstrain, lower defect density, higher E_a and higher resistivity than $Pb_2CuGly_2Br_4$ SC. As a result, the $Pb_2CuGly_2Cl_4$ SC-based X-ray detector displays a high sensitivity of 9,250 μC Gy^{-1} cm^{-2}. Meanwhile, the detector presents excellent operating stability under a high electric field (120 V mm^{-1}) and continuous X-ray irradiation along with an extremely low dark current drift of 1.20×10^{-9} nA mm^{-1} s^{-1} V^{-1}. In addition, an aqueous paste based on $Pb_2CuGly_2Cl_4$ nanocrystal is prepared, and it

 https://doi.org/10.1007/s40820-025-01788-z

is blade-coated on thin-film transistor (TFT) array substrate, achieving an X-ray imaging panel with spatial resolution of 2.2 lp mm^{-1}.

2 Experimental Section

2.1 Materials

Lead chloride ($PbCl_2$, 99%), copper bromide ($CuBr_2$, 99%), anhydrous copper chloride (anhydrous $CuCl_2$, 98%) and glycine (NH_2CH_2COOH, 99%) were purchased from Aladdin Reagent Ltd. Lead bromide ($PbBr_2$, 99%) was purchased from Shanghai Maclin Biochemical Technology Co., LTD. All materials were used without further purification.

2.2 Preparation of $Pb_2CuGly_2Br_4$ and $Pb_2CuGly_2Cl_4$ SCs

2.2.1 Preparations of the $Pb_2CuGly_2Br_4$ SC

0.3763 g lead bromide ($PbBr_2$), 0.446 g copper bromide ($CuBr_2$) and 0.3754 g glycine (NH_2CH_2COOH), with a molar ratio of 1:2:5, were dissolved in 90 mL distilled water and magnetically stirred at 100 °C for 30 min. The precursor solution was then rapidly evaporated at 100 °C for 24 h to form some micron-scale SCs. Thereafter, the supersaturated solution was rapidly filtered into a 20-mL vial and a small seed crystal was added to the supersaturated solution. After slow evaporation at 50 °C for 14 days, a large-sized $Pb_2CuGly_2Br_4$ SC was obtained.

2.2.2 Preparations of the $Pb_2CuGly_2Cl_4$ SC

Similar to the preparation process of $Pb_2CuGly_2Cl_4$ SC, 0.135 g anhydrous copper chloride (anhydrous $CuCl_2$), 0.556 g lead chloride ($PbCl_2$) and 0.7507 g glycine (NH_2CH_2COOH), with a molar ratio of 1:2:10, were dissolved in 60 mL distilled water and magnetically stirred at 100 °C for 30 min. The perovskite precursor solution was then rapidly evaporated at 100 °C for 24 h to form some micron-scale nucleus. Afterward, the supersaturated solution was rapidly filtered into a 20-mL vial and a small seed crystal was added to the solution. After slow evaporation at 50 °C for 14 days, a high-quality $Pb_2CuGly_2Cl_4$ SC could be obtained.

2.3 Device Fabrication

Firstly, the upper and bottom surfaces of the SCs was polished by using the grinding papers to remove the surface residue and defects. The thicknesses of the polished $Pb_2CuGly_2Cl_4$ and $Pb_2CuGly_2Br_4$ SCs were 1 and 0.8 mm, respectively. Then we fabricated the X-ray detectors with a Cu/SC/Cu vertical structure. The Cu electrodes with a thickness of about 60 nm were deposited on the both sides of the SCs by the thermal evaporation method, and the device area was controlled to be 1 mm^2.

2.4 $Pb_2CuGly_2Cl_4$ TFT Array Detector Fabrication

Firstly, the $Pb_2CuGly_2Cl_4$ SCs were grinded to powder. Then, the $Pb_2CuGly_2Cl_4$ precursor paste with the concentration of 3.3 g mL^{-1} was obtained by directly dispersing $Pb_2CuGly_2Cl_4$ in water. Finally, the $Pb_2CuGly_2Cl_4$ paste was blade-coated on the TFT array followed by annealed 100 °C for 20 min to remove the residual water, and an Au electrode with thickness of 80 nm was deposited on $Pb_2CuGly_2Cl_4$ film by thermal evaporation.

2.5 Characterization of Materials

The single-crystal data of $Pb_2CuGly_2X_4$ (X = Cl, Br) SCs were obtained from the previous literature [27]. The corresponding crystal structures of $Pb_2CuGly_2X_4$ (X = Cl, Br) SCs were solved by the VESTA software. The powder X-ray diffraction (XRD) patterns of $Pb_2CuGly_2X_4$ (X = Cl, Br) were performed by the D8-ADVANCE X-ray diffractometer with a Cu Kα radiation (λ = 1.54056 Å). The XRD data were collected at 293 K with a scan speed of 5° min^{-1} from 5° to 50°. The thermogravimetric analysis (TGA) was performed under a TA SDT650 instrument. 10 mg $Pb_2CuGly_2X_4$ (X = Cl, Br) powder samples was placed in an alumina crucible followed by heated from 20 to 800 °C at a heating rate of 10 °C min^{-1} under an atmosphere of air. The UV–Vis–NIR absorbance spectra of $Pb_2CuGly_2X_4$ (X = Cl, Br) crystal powder were obtained with a Cary 5000 UV–Vis–NIR spectrophotometer. The high-resolution ultraviolet photoelectron spectroscopy

(UPS) was measured by an integrated vacuum system equipped with a multi-technique surface analysis system (VG ESCALAB MK II spectrometer).

2.6 Detector Performance Measurement

The bulk resistivity of $Pb_2CuGly_2X_4$ (X = Cl, Br) SC detector was obtained by fitting the dark I–V curves obtained via a semiconductor parameter analyzer (PDA SC-PRO 7). For X-ray characterization, an anode X-ray tube (NE-X) was utilized the source. The tube acceleration voltage of the X-ray source was fixed at 50 kV_p, and the emitted X-ray dose rates were adjusted from 160 to 1620 μGy s^{-1} by controlling the operational current. The radiation dose rate was calibrated by using a commercial X-ray dosimeter from Germany. The both perovskitoid SC detectors were tested under different applied bias, and the response current of the detector was recorded via the PDA SC-PRO 7. As for the imaging test, a TFT array substrate (LZ-03AMR) was used to acquire the images of the target quickly.

3 Results and Discussion

3.1 Crystal Structure of $Pb_2CuGly_2X_4$ (X = Cl, Br)

Figure 1a demonstrates the growth schematic of the perovskitoid SCs based on traditional solvent evaporation method according to a previous literature [27]. In brief, the PbX_2, CuX_2 (X = Cl, Br) and glycine were completely dissolved in water at 100 °C; then, the solution was rapidly volatilized for 24 h to form numerous seed crystals. Subsequently, the supersaturated solutions were filtered, and one seed crystal was transferred to the supersaturated solutions for further growth. After slow evaporation at 50 °C for 14 days, the large-sized perovskitoid SCs were obtained. Figure 1b gives the photographs of $Pb_2CuGly_2Br_4$ SC and $Pb_2CuGly_2Cl_4$ SC with the dimension sizes of about 4 mm × 3 mm × 1.2 mm and 3 mm × 2 mm × 0.7 mm, and the $Pb_2CuGly_2Br_4$ SC exhibits dark blue, while the $Pb_2CuGly_2Cl_4$ displays light blue. The $Pb_2CuGly_2X_4$ (X = Cl, Br) crystallizes in the $P2_1/c$ group, and the detailed crystallographic information is presented in Table S1. As for the crystal structure of $Pb_2CuGly_2Cl_4$, one copper ion (Cu^{2+}) coordinated with two deprotonated Gly via amine groups and carboxylate groups to form robust $CuGly_2$ symmetric unit, where the non-hydrogen atoms approximately are on a plane and the Cu^{2+} is located at the center of the unit. Then the lead chlorine layers are linked by the $CuGly_2$ through Pb–O bonds to form the 3D frameworks (Fig. 1c), which is different from the traditional 3D perovskite structure. It should be noted that the lead atoms are surrounded by five chlorine atoms and three oxygen atoms to construct a $[PbCl_5O_3]^{9-}$ dodecahedron (Fig. S2). Then these dodecahedrons build the inorganic layer via the face-sharing and edge-sharing connection (Fig. 1d). Except for the $CuGly_2$ pillars, the robust inorganic networks enabled by face/edge-sharing also can significantly suppress the ion migration [17], which is conductive to inhibiting the dark current drift of the device. Figure 1e exhibits the (011) plane of the $Pb_2CuGly_2Cl_4$ SC. The crystal structure of $Pb_2CuGly_2Br_4$ is similar to $Pb_2CuGly_2Cl_4$, and the detail structure of $Pb_2CuGly_2Br_4$ is listed in the Fig. S1.

The XRD patterns of $Pb_2CuGly_2X_4$ (X = Cl, Br) powder and SCs are well matched with their simulated ones obtained from single-crystal structure data [27]. In addition, the $Pb_2CuGly_2X_4$ SCs show three strong diffraction peaks (0ll) (l = 1, 2, 3), implying their good crystallographic orientation along the (0ll) plane (Fig. 1f). It is worth noting that the (0ll) plane diffraction peaks of $Pb_2CuGly_2Cl_4$ SC shift to the larger angles compared with $Pb_2CuGly_2Br_4$ SC, conforming a smaller lattice constant of $Pb_2CuGly_2Cl_4$ SC. The microstrain (ε) of $Pb_2CuGly_2X_4$ SCs was calculated according to the XRD patterns by the Williamson–Hall equation [29]:

$$\beta\cos\theta = k\lambda/D + 4\varepsilon\sin\theta \quad (1)$$

where β, θ, k, λ and D represent the full width at half maximum (FWHM), Bragg's diffraction angle, Scherrer constant, the wavelength of the X-ray and average crystallite size, respectively. The ε can be derived from the slope of the fitting line (Fig. S3). The $Pb_2CuGly_2Cl_4$ exhibits smaller ε of 0.02 than $Pb_2CuGly_2Br_4$ (0.07), indicating better crystalline quality of $Pb_2CuGly_2Cl_4$ SC with lower crystal defect density. Subsequently, the thermogravimetric analysis (TGA) of $Pb_2CuGly_2X_4$ (X = Cl, Br) powder was performed in Fig. S4. $Pb_2CuGly_2Cl_4$ begins to decompose at 198 °C, exhibiting a similar decomposition temperature with that of $Pb_2CuGly_2Br_4$ (194 °C). This is can be ascribed to the melting of the $CuGly_2$ clusters [27].

https://doi.org/10.1007/s40820-025-01788-z

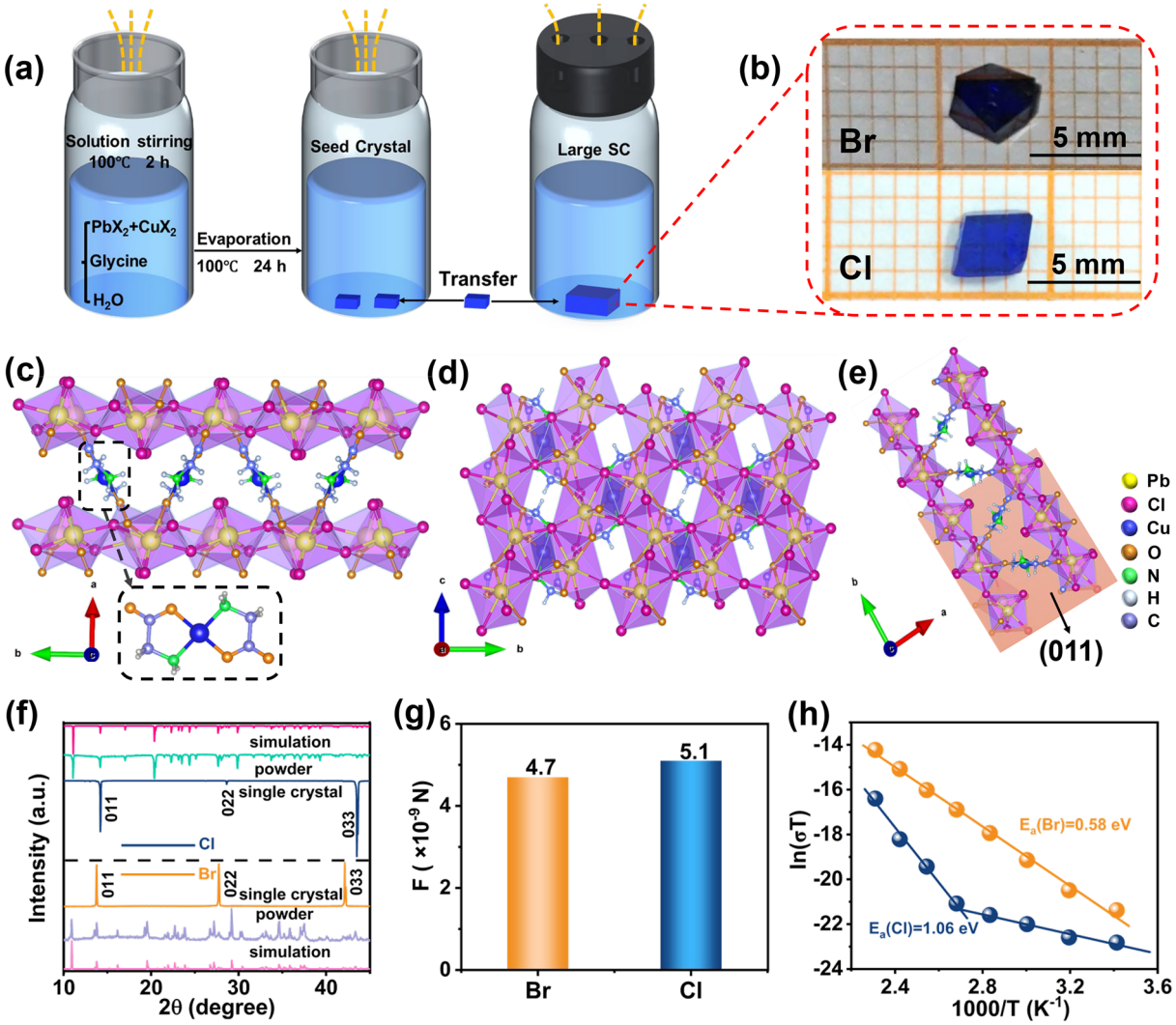

Fig. 1 **a** Growth schematic of $Pb_2CuGly_2X_4$ (X = Cl, Br). **b** Photographs of $Pb_2CuGly_2X_4$ (X = Cl, Br) SCs. **c, d, e** Crystal structure of $Pb_2CuGly_2Cl_4$ observed along c axis and a axis, respectively, and the (011) crystal plane. **f** XRD patterns of $Pb_2CuGly_2X_4$ (X = Cl, Br) SC and powder. **g** Comparison of the electrostatic interaction force between Pb^{2+} and halide anions X^- (X = Cl, Br). **h** Temperature-dependent conductivity of $Pb_2CuGly_2X_4$ (X = Cl, Br) SC devices

The ideal X-ray detection materials should possess suppressed ion migration under large applied bias to maintain the stable output of the photocurrent. To assess the ion migration in the $Pb_2CuGly_2X_4$ SCs, the individual electrostatic interaction force between the lead cations and halide ions was calculated according to the Coulomb's law. The corresponding ionic radii and valence states are listed in Table S2, and Fig. S5 exhibits the schematic diagram of the electrostatic interaction force. As shown in Fig. 1g, the Cl^- has a stronger interaction with Pb^{2+} (5.1×10^{-9} N) than the Br^- (4.7×10^{-9} N) owing to its smaller ionic radii, which may results in inhibited ion migration so as to enhanced operating stability for $Pb_2CuGly_2Cl_4$ SC detector. Furthermore, we conducted the temperature-dependent conductivity measurement to compare the ion migration activation energy (E_a) of the two SCs (Fig. 1h). The E_a can be calculated according to the Nernst–Einstein equation [24]:

$$\sigma(T) = \frac{\sigma_0}{T}\exp\left(\frac{-E_a}{k_B T}\right) \quad (2)$$

where the σ represents the measured conductivity of the SCs under different temperature, σ_0 is a constant and the

k_B reflects the Boltzmann constant. The calculated E_a of $Pb_2CuGly_2Cl_4$ and $Pb_2CuGly_2Br_4$ SC are 1.06 eV and 0.58 eV, respectively, which is in accord with the results concluded from Fig. 1f, g. The higher E_a of $Pb_2CuGly_2Cl_4$ allows the utilization of large bias to drive the carrier transport without sacrificing the detector operating stability.

3.2 Optoelectronic Properties of $Pb_2CuGly_2X_4$ (X = Cl, Br)

The band structure of $Pb_2CuGly_2X_4$ (X = Cl, Br) was explored by density functional theory (DFT) calculations, and the detailed calculated method is presented in supporting information. As shown in Fig. 2a, b, the top valence band is a flat band for $Pb_2CuGly_2X_4$ (X = Cl, Br), and both $Pb_2CuGly_2Br_4$ and $Pb_2CuGly_2Cl_4$ are direct semiconductors with a calculated band gap of 2.94 and 3.12 eV, respectively. Such band gaps are consistent with the blue color of the crystals. It should be noted that the calculated band gap of $Pb_2CuGly_2Br_4$ in this work is relative lower than that (3.37 eV) reported in reference [29] along with the difference in their electronic band structures [29], which may be attributed to the different level theory employed. According to the calculated density of states (DOS) spectra of $Pb_2CuGly_2X_4$ (X = Cl, Br), the Pb 5*d* orbital mainly accounts for the conduction band minimum (CBM) of $Pb_2CuGly_2X_4$ (X = Cl, Br), whereas the Cu 3*d* and O 2*p* orbitals mainly dominate the corresponding valence band maximum (VBM). This clearly declares that $CuGly_2$ species can participate the carrier's transport. Afterward, we measured the optical E_g of $Pb_2CuGly_2X_4$ (X = Cl, Br) by the ultraviolet–visible–near infrared (UV–Vis–NIR) absorbance spectrum (Fig. 2c). It can be seen that $Pb_2CuGly_2X_4$ (X = Cl, Br) exhibits a broad absorption range from visible to near infrared region, where the high energy absorption originates from the matrix absorption, and the low energy absorption is due to the *d*–*d* transitions of Cu^{2+} [29]. The blue color of the $Pb_2CuGly_2X_4$ (X = Cl, Br) SC can be attributed to the d–d transitions of Cu^{2+} [27, 28]. Based on the matrix absorption, the optical E_g of $Pb_2CuGly_2X_4$ (X = Cl, Br) is calculated to be 3.52 and 3.21 eV, respectively. The

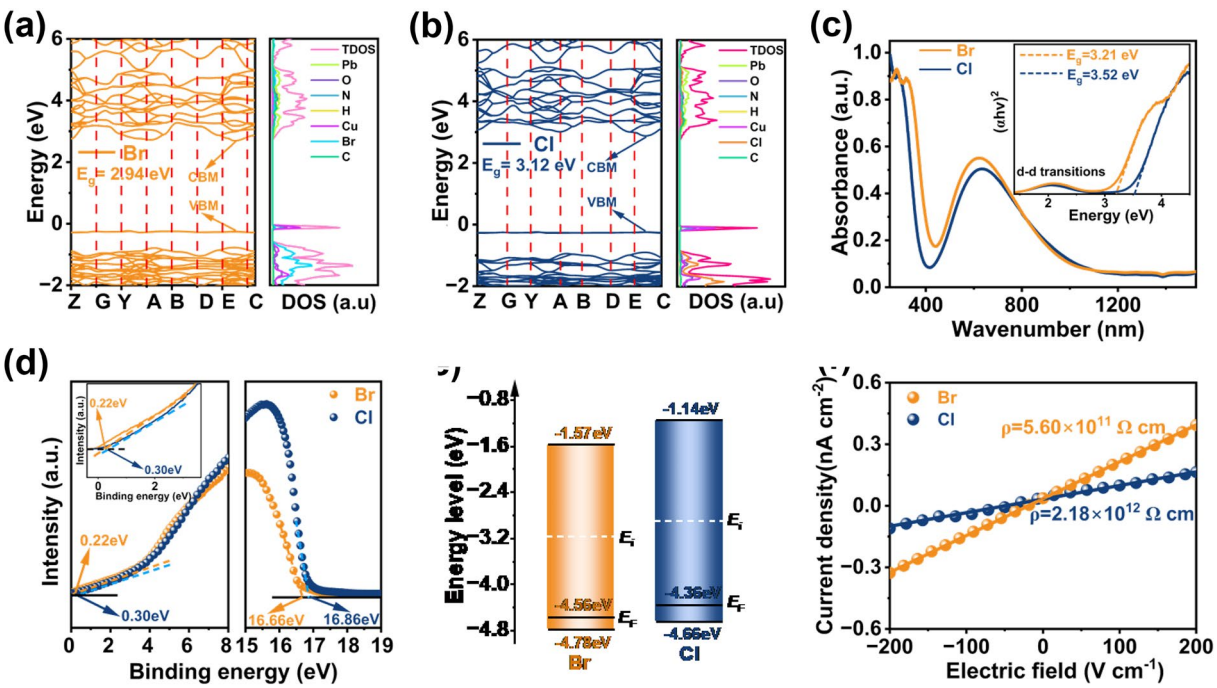

Fig. 2 **a** Band structure and DOS simulation of $Pb_2CuGly_2Br_4$. **b** Band structure and DOS simulation of $Pb_2CuGly_2Cl_4$. **c** UV–Vis–NIR absorbance spectra of $Pb_2CuGly_2X_4$ (X = Cl, Br) single-crystal powder, and the inset is the corresponding Taus plots. **d** UV photoelectron spectroscopy of $Pb_2CuGly_2X_4$ (X = Cl, Br) and the partial enlarged detail (inset). **e** Energy level diagram of $Pb_2CuGly_2X_4$ (X = Cl, Br). **f** Dark current density as a function of the electric field for $Pb_2CuGly_2X_4$ (X = Cl, Br) SC X-ray detectors

https://doi.org/10.1007/s40820-025-01788-z

actual value of the band gap is always higher than that derived from DFT calculation, which has been widely accepted owing to the limitation of the employed model. The calculated E_g of $Pb_2CuGly_2Br_4$ is in accord with that (3.25 eV) in reference [29]. The luminescent properties of $Pb_2CuGly_2X_4$ (X = Cl, Br) SC are also investigated. As shown in Fig. S6, the $Pb_2CuGly_2X_4$ (X = Cl, Br) SC under the illumination of 310 nm ultraviolet (UV) light exhibits no fluorescence except for their intrinsic blue color, and the fluorescence emission peak of $Pb_2CuGly_2X_4$ (X = Cl, Br) single crystals is absent in the range of 320–600 nm, 640–850 nm under the excitation of 310 nm UV light, indicating no fluorescence emission. Then the UV photoelectron spectroscopy (UPS) measurements were taken to further estimate the energy level of $Pb_2CuGly_2X_4$ (X = Cl, Br) (Fig. 2d). It illustrates that the work function of $Pb_2CuGly_2X_4$ (X = Cl, Br) is −4.36 and −4.56 eV, respectively, from the secondary electron cutoff edge of the spectrum, and the valence band of $Pb_2CuGly_2X_4$ (X = Cl, Br) is 0.3 and 0.22 eV below the Fermi level, respectively. Based on the results of UPS spectrum and absorption spectra, the VBM and CBM of $Pb_2CuGly_2X_4$ (X = Cl, Br) are located at −4.66/−4.78 eV and −1.14/−1.57 eV, respectively (Fig. 2e). Since the Fermi levels of $Pb_2CuGly_2X_4$ (X = Cl, Br) are lower than the middle positon of forbidden band, that indicates the $Pb_2CuGly_2X_4$ (X = Cl, Br) are p-type semiconductors. Subsequently, the resistivity of $Pb_2CuGly_2X_4$ (X = Cl, Br) SC was characterized. As shown in Fig. 2f, the resistivity of $Pb_2CuGly_2X_4$ (X = Cl, Br) is derived to be 2.18×10^{12} and 5.6×10^{11} Ω cm, respectively, which is much higher than that of 3D perovskites like $MAPbI_3$, $MAPbBr_3$, $FAPbI_3$, etc. [31, 32]. The higher resistivity of $Pb_2CuGly_2Cl_4$ can be assigned to the higher crystal quality and suppressed ion migration, which is essential to reduce the detector noise.

3.3 Performance of $Pb_2CuGly_2X_4$ SC X-ray Detector

We constructed the X-ray detector with device configuration of Cu/$Pb_2CuGly_2X_4$ (X = Cl, Br) SC/Cu to estimate their detection performance. The working mechanism of the detector is rendered in Fig. 3a. When the detector absorbs the X-ray photons, numerous electron–hole pairs are generated, then these electron–hole pairs separate and transport across the semiconductors under the applied bias, and finally be collected by the electrodes. Figure 3b compares the X-ray attenuation coefficients of $Pb_2CuGly_2X_4$ (X = Cl, Br) SC with other semiconductors like CdTe, α-Se, $MAPbBr_3$ and $CsPbBr_3$ over a broad photon energy region ranging from 10 to 10^3 keV by using the NIST database [33]. When the X-ray photon energy ranges from 100 eV to 1000 keV, the X-ray absorption coefficients of $Pb_2CuGly_2X_4$ (X = Cl, Br) are higher than that of CdTe and α-Se, and comparable to $MAPbBr_3$ and $CsPbBr_3$, exhibiting a strong X-ray stopping power. The high sensitivity of X-ray detectors depends on the efficient charge collection. To character the important physical property, the $\mu\tau$ products of the $Pb_2CuGly_2X_4$ (X = Cl, Br) SC detector, reflecting the average carrier drift distance per unit electric field, were derived by fitting the photoconductivity of $Pb_2CuGly_2X_4$ (X = Cl, Br) SC detector under the X-ray illumination and applied bias according to the modified Hecht equation [34]:

$$I = \frac{I_0 \mu\tau V}{L^2} \frac{1 - \exp\left(-\frac{L^2}{\mu\tau V}\right)}{1 + \frac{Ls}{V\mu}} \quad (3)$$

where the I_0 denotes the saturated photocurrent, V is the applied bias, L represents the thickness of the $Pb_2CuGly_2X_4$ (X = Cl, Br) SC and the s is the surface recombination velocity. The $\mu\tau$ product of $Pb_2CuGly_2Cl_4$ SC detector is determined to be 3.65×10^{-4} cm^2 V^{-1}, which is higher than that (1.86×10^{-4} cm^2 V^{-1}) of the $Pb_2CuGly_2Br_4$ SC detector (Fig. 3c). Therefore, the higher $\mu\tau$ product of $Pb_2CuGly_2Cl_4$ SC device will result in a higher X-ray detection performance. Then, the relative dielectric constants (ε) of $Pb_2CuGly_2X_4$ (X = Cl, Br) SC were assessed from the capacitance–frequency curves, as shown in Fig. S7. The ε values of $Pb_2CuGly_2X_4$ (X = Cl, Br) SC are calculated to be 32 and 24, respectively. According to the Wannier–Mott exciton equation [35], the exciton binding energy (E_b) is inversely proportional of the ε^2. This demonstrates that $Pb_2CuGly_2Cl_4$ may possess lower E_b compared to $Pb_2CuGly_2Br_4$, facilitating the separation of electron–hole pairs. As discussed above, the $Pb_2CuGly_2Cl_4$ SC shows smaller microstrain than $Pb_2CuGly_2Br_4$ SC, implying lower trap density. To further confirm the speculation, we estimated the trap density (n_{trap}) of $Pb_2CuGly_2X_4$ (X = Cl, Br) SC by a space-charge-limited currents (SCLC) measurements in Fig. 3d. The $Pb_2CuGly_2Cl_4$ SC presents lower n_{trap} (2.1×10^{10} cm^{-3}) than

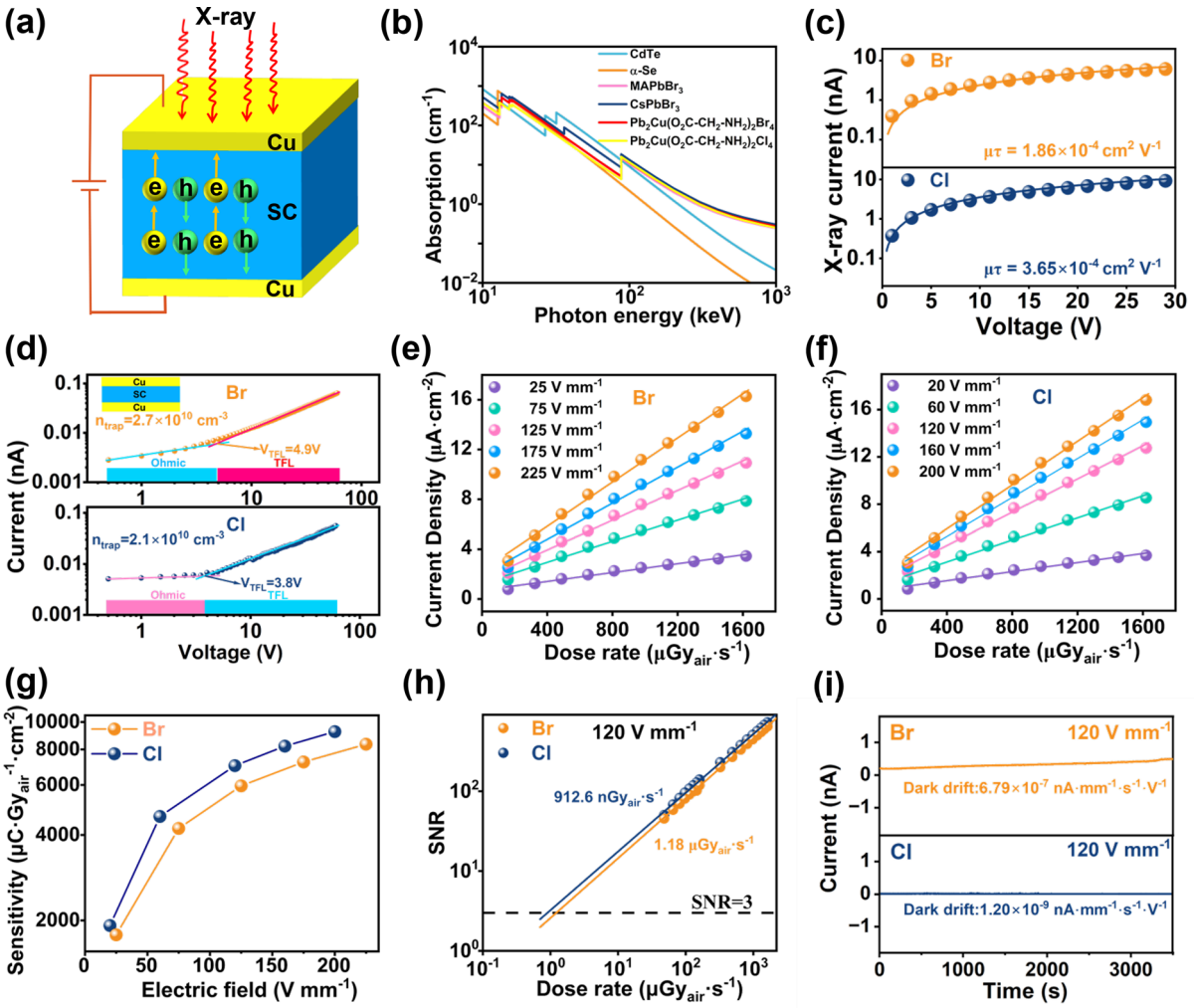

Fig. 3 **a** Schematic of detector structure and working mechanism. **b** Absorption coefficient of CdTe, α-Se, $Pb_2CuGly_2X_4$ (X = Cl, Br), $MAPbBr_3$ and $CsPbBr_3$. **c** $\mu\tau$ product measurement of $Pb_2CuGly_2X_4$ (X = Cl, Br) SC. **d** Dark current–voltage characteristics of $Pb_2CuGly_2X_4$ (X = Cl, Br) SC detector measured by the SCLC method, inset is the device structure. **e** Photocurrent density of $Pb_2CuGly_2Br_4$ SC detector under various dose rates. **f** Photocurrent density of $Pb_2CuGly_2Cl_4$ SC detector under various dose rates. **g** Sensitivity of $Pb_2CuGly_2X_4$ (X = Cl, Br) SC detector under different electric fields. **h** SNR of the $Pb_2CuGly_2X_4$ (X = Cl, Br) SC detector at different dose rates with a fixed electric field of 120 V mm^{-1}. **i** Dark current stability measurement of $Pb_2CuGly_2X_4$ (X = Cl, Br) SC detector at the electric field of 120 V mm.$^{-1}$

that of $Pb_2CuGly_2Br_4$ SC (2.7×10^{10} cm^{-3}). The lower n_{trap} in $Pb_2CuGly_2Cl_4$ SC is beneficial to restrain carrier recombination, thereby contributing to enhanced charge collection efficiency. In addition, the as-prepared $Pb_2CuGly_2Br_4$ SC gives lower trap density in comparison with that (7.55×10^{10} cm^{-3}) in the literature [29], indicating the improved crystal quality of $Pb_2CuGly_2Br_4$ SC in this work.

The $Pb_2CuGly_2X_4$ (X = Cl, Br) SC detectors exhibit an ideal linear photocurrent response with the varied X-ray dose rates from 160 to 1620 μGy s^{-1} under different electric field as in Figs. S8 and S9, and the sensitivity of $Pb_2CuGly_2Cl_4$ SC detector is determined to be 1920, 4650, 7020, 8220 and 9250 μC Gy^{-1} cm^{-2} at the electric fields of 20, 60, 120, 160 and 200 V mm^{-1}, respectively, according to the quantitative liner regression analyses (Fig. 3f). As a contrast, the $Pb_2CuGly_2Br_4$ SC detector delivers lower sensitivities of 1780, 4220, 5960, 7230 and 8350 μC Gy^{-1} cm^{-2} under electric fields of 25, 75, 125, 175 and 225 V mm^{-1} than $PbCuGly_2Cl_4$ SC detector in Fig. 3e. It is worth noting that the sensitivity of our $Pb_2CuGly_2Br_4$ SC detector is higher than that (1462.7 μC Gy^{-1} cm^{-2}, 50 V mm^{-1}) reported in the literature [29], which is consistent with the result of Fig. 3d. Furthermore,

https://doi.org/10.1007/s40820-025-01788-z

we compared the detection efficiency of the both detectors. The theoretical sensitivity (S_0) of $Pb_2CuGly_2X_4$ (X = Cl, Br) SC detector for 50 keV X-ray is estimated to be 4.85×10^3 and 4.82×10^3 μC Gy^{-1} cm^{-2}, respectively. The detailed calculation information is provided in the experimental section. Thereby, the detection efficiency of $Pb_2CuGly_2Cl_4$ SC detector under 120 V mm^{-1} is calculated to be 145% by S/S_0, higher than that of $Pb_2CuGly_2Br_4$ SC detector (~124%). It should be pointed out that both detectors present a trend that the sensitivity increases with the increase in the electric field due to the enhanced carrier collection efficiency (Fig. 3g). Thereby, higher sensitivity are supposed to be achieved once further increasing the electric field. We further compare the sensitivity of $Pb_2CuGly_2Cl_4$ SC detector with other semiconductors like α-Se, 2D and 3D perovskite SCs (Table S3). The sensitivity of $Pb_2CuGly_2Cl_4$ SC detector at 200 V mm^{-1} is over 21 times higher than that of commercial α-Se at 15,000 V mm^{-1} (440 μC Gy^{-1} cm^{-2}) [36], demonstrating a promising application prospect. Although the sensitivity of $Pb_2CuGly_2Cl_4$ SC detector is much larger than that of the reported 2D perovskite SCs such as (DGA) PbI_4 (4,869 μC Gy^{-1} cm^{-2} @ 1,200 V mm^{-1}) and (4AEPy) PbI_4 (5,627μC Gy^{-1} cm^{-2}@ 200 V mm^{-1}) [19, 20], it is still behind the traditional 3D perovskite SCs like $CsPbBr_3$ and $FAPbI_3$ [3, 11], which is caused by the unique crystal structure of $Pb_2CuGly_2Cl_4$ SC.

The low detection limit of the detector is a primary parameter of high-performance detector that determines the lowest detectable X-ray dose rates. According to the International Union of Pure and Applied Chemistry, the dose rate can be viewed the lowest detection limit when the signal-to-noise ratios (SNR) is 3 [37]. Therefore, we calculate the SNR of the $Pb_2CuGly_2X_4$ (X = Cl, Br) SC detector at different dose rates with a fixed electric field of 120 V mm^{-1} followed by extending the fitting line to SNR = 3 (Fig. 3h). The detailed current density data used for calculating the detection limit of $Pb_2CuGly_2X_4$ (X = Cl, Br) SC detector are provided in Fig. S10. The derived lowest detectable dose rate of $Pb_2CuGly_2Cl_4$ SC detector is 912.6 nGy s^{-1}, lower than that of $Pb_2CuGly_2Br_4$ SC detector (1.18 μGy s^{-1}), implying the excellent detection ability of $Pb_2CuGly_2Cl_4$ SC at lower dose rate. The relative high detection limit of $Pb_2CuGly_2X_4$ (X = Cl, Br) SC detectors can be ascribed to the defect-induced unstable time-resolved current density.

The large electric field always causes serious dark current drift of detector due to the well-known ion migration in perovskites. To inspect the dark current stability of $Pb_2CuGly_2X_4$ (X = Cl, Br) SC detector, we applied an electric field of 120 V mm^{-1} on both detectors for 3,500 s. As shown in Fig. 3i, $Pb_2CuGly_2Cl_4$ SC device shows lower dark current under 120 V mm^{-1} due to its larger bulk resistivity. In addition, the $Pb_2CuGly_2Cl_4$ SC detector gives a lower dark current drift (I_{drift}) of 1.20×10^{-9} nA mm^{-1} s^{-1} V^{-1} than that of $Pb_2CuGly_2Br_4$ SC detector (6.79×10^{-7} nA mm^{-1} s^{-1} V^{-1}), demonstrating higher dark current stability. The low I_{drift} of $Pb_2CuGly_2Cl_4$ SC originates from stronger electrostatic interaction force, higher E_a and lower n_{trap}, which can effectively suppress the dark current noise.

The photocurrent response stability of the X-ray detector under pulsed X-ray irradiation is also a concern that should be cared. As illustrated in Fig. 4a, the $Pb_2CuGly_2Cl_4$ SC detector displays stable photocurrent and dark current response with nearly no change during the whole measurement period of 4,000 s under the electric field of 120 V mm^{-1}, suggesting an unprecedented X-ray response stability. In addition, we further tested the operating stability of the $Pb_2CuGly_2Cl_4$ SC detector under continuous X-ray irradiation (810 μGy s^{-1}) with the electric field of 120 V mm^{-1}. As shown in Fig. 4b, the response current of $Pb_2CuGly_2Cl_4$ SC detector almost maintains the initial photocurrent value after continuous work for over 3,500 s along with exposure to a total X-ray does of 2.86 Gy, which is equal to about 2.86×10^4 exposure times of the standard commercial X-ray chest radiograph (~0.1 mGy per exposure) [38]. Similar to the estimation of dark current drift, the $Pb_2CuGly_2Cl_4$ SC detector exhibits a photocurrent drift of 2.63×10^{-8} nA mm^{-1} s^{-1} V^{-1}, indicating an excellent X-ray operating stability of the detector under the harsh working conditions. Finally, the long-term air stability test of $Pb_2CuGly_2Cl_4$ SC detector was carried out. As shown Fig. 4c, the $Pb_2CuGly_2Cl_4$ SC detector stored in air for one week without any encapsulation still exhibits no signal attenuation under the dose rate of 810 μGy s^{-1} at 120 V mm^{-1}, demonstrating the excellent air stability of $Pb_2CuGly_2Cl_4$ SC detector. Based on these excellent performances, the $Pb_2CuGly_2Cl_4$ SC detector is expected to be suitable for high-quality X-ray imaging.

3.4 X-ray Imaging of $Pb_2CuGly_2Cl_4$ TFT Array Detector

To meet the X-ray imaging practical application, developing integrated X-ray array detector is imperative.

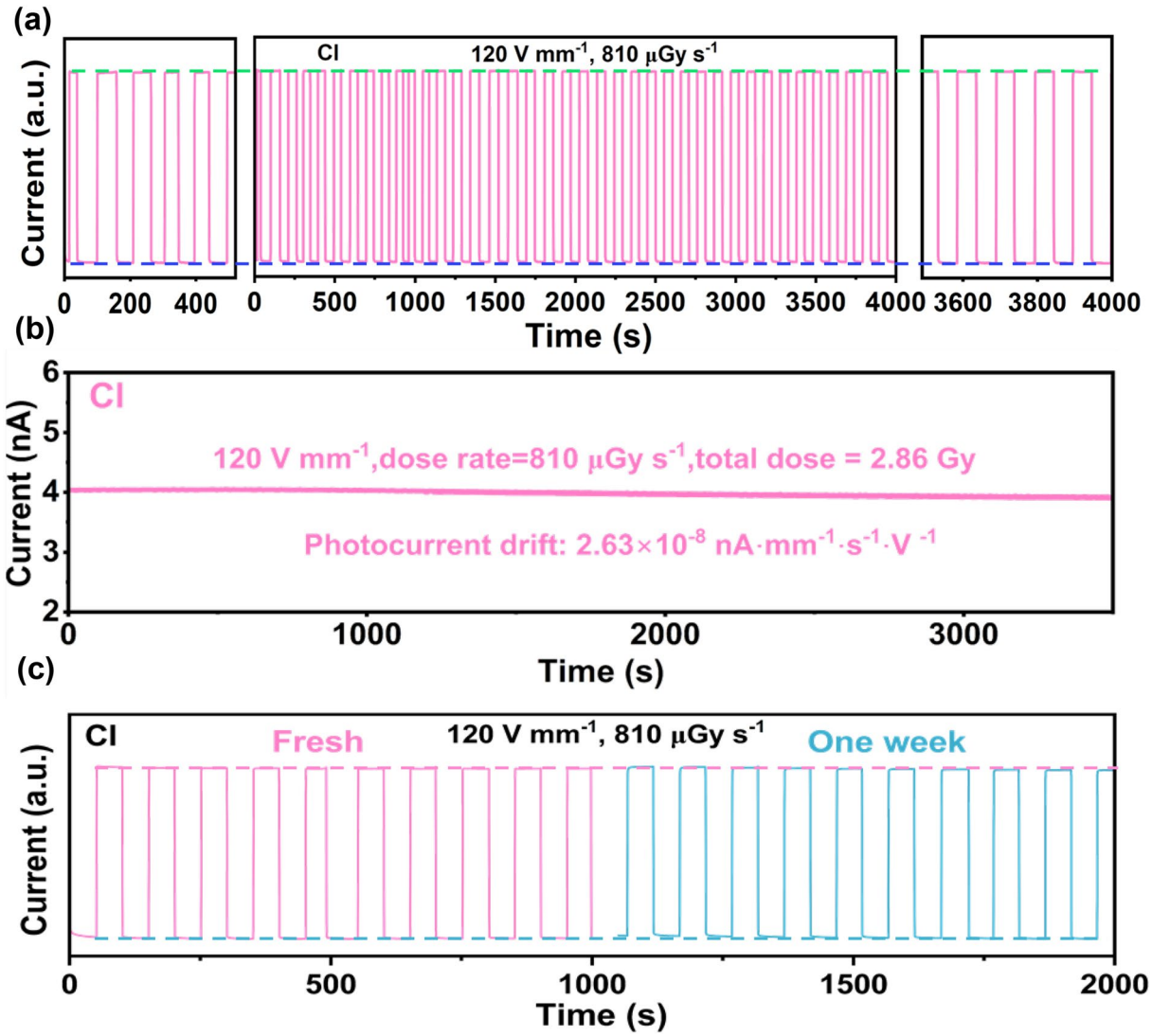

Fig. 4 Response current of $Pb_2CuGly_2Cl_4$ SC detector **a** under a pulsed X-ray irradiation at the electric field of 120 V mm^{-1} and **b** under continuous X-ray irradiation at the electric field of 120 V mm^{-1}. **c** Air stability test of $Pb_2CuGly_2Cl_4$ SC detector

Considering the crystallization of $Pb_2CuGly_2Cl_4$ SC in water, we prepared the $Pb_2CuGly_2Cl_4$ aqueous paste by dispersing $Pb_2CuGly_2Cl_4$ nanocrystal in water (Fig. S11). The $Pb_2CuGly_2Cl_4$ paste was directly blade-coated onto the TFT array with pixel size of 200 × 200 μm^2 (64 × 64 pixels), and the $Pb_2CuGly_2Cl_4$ precursor film was heated at 100 °C to remove the residual water. Finally, a gold electrode was evaporated on the $Pb_2CuGly_2Cl_4$ thick film (Fig. S12). As shown in Fig. 5a, the thickness of the $Pb_2CuGly_2Cl_4$ thick film was about 1 mm. The XRD patterns of $Pb_2CuGly_2Cl_4$ film is provided in the Fig. S13. It is discovered that the diffraction peak of $Pb_2CuGly_2Cl_4$ film is consistent with that of the $Pb_2CuGly_2Cl_4$ powder and the simulation, indicating no new phases or substances are formed during the film preparation process. This also confirms the excellent stability of $Pb_2CuGly_2Cl_4$ powder in water. Figure 5b displays the photograph of the $Pb_2CuGly_2Cl_4$ TFT array detector, and the microphotograph of the different region of TFT array is given in Fig. S14. Firstly, the X-ray detection performance of $Pb_2CuGly_2Cl_4$ TFT array detector was studied. As shown in Fig. S15, the $Pb_2CuGly_2Cl_4$ film TFT detector also exhibited an ideal linear photocurrent response with the varied X-ray dose rate under different applied bias, yielding a sensitivity of 1490, 2430, 3220, 3830 and 4490 μC Gy^{-1} cm^{-2} at the electric field of 20, 40, 60, 80 and 100 V mm^{-1}(Fig. 5c, d). Compared with the $Pb_2CuGly_2Cl_4$ SC detector, the

 https://doi.org/10.1007/s40820-025-01788-z

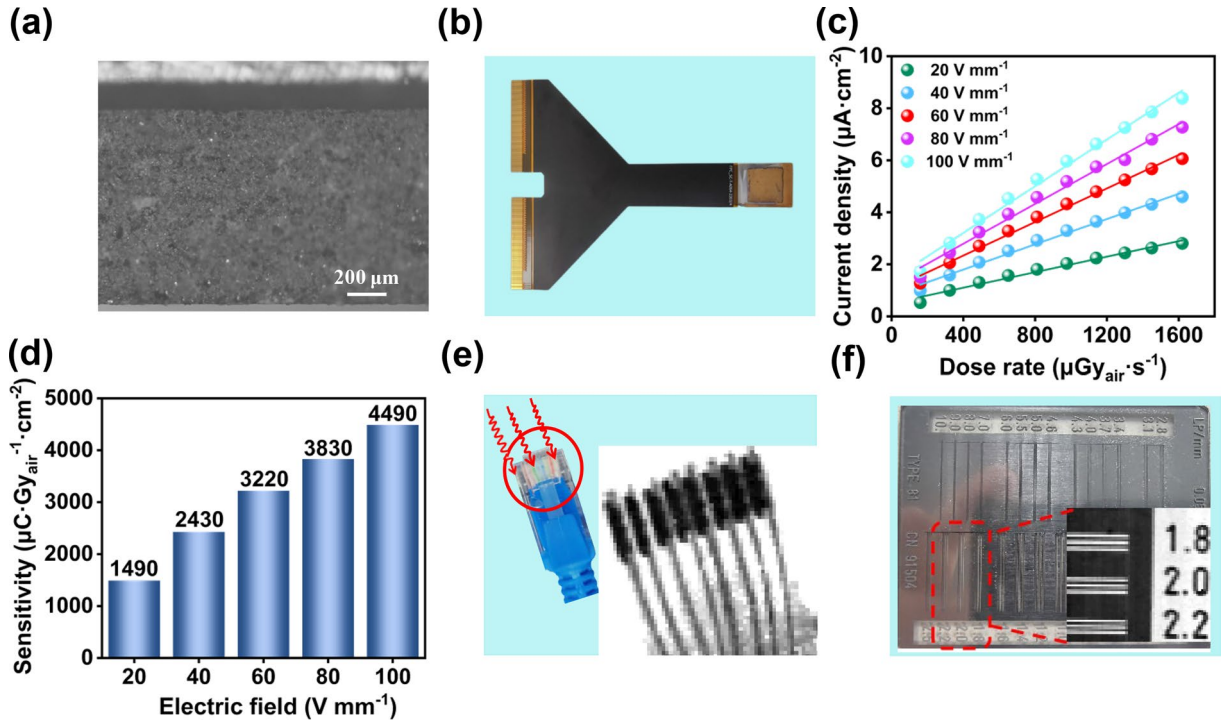

Fig. 5 **a** Cross-sectional SEM of $Pb_2CuGly_2Cl_4$ film. **b** Photograph of the $Pb_2CuGly_2Cl_4$ TFT array detector. **c** Photocurrent density of $Pb_2CuGly_2Cl_4$ TFT array detector under various dose rates at different electric field. **d** Sensitivity of $Pb_2CuGly_2Cl_4$ TFT array detector under different electric field. **e** Optical photograph of the network cable plug and the corresponding X-ray image. **f** X-ray image of the lead line pair card

$Pb_2CuGly_2Cl_4$ TFT array detector gives lower sensitivity, which can be owing to the defects in $Pb_2CuGly_2Cl_4$ polycrystalline film. Therefore, further optimizing the quality of $Pb_2CuGly_2Cl_4$ film is expected to improve the sensitivity of $Pb_2CuGly_2Cl_4$ TFT array detector.

Subsequently, we further performed the X-ray imaging study. A network cable plug is selected as the target for X-ray imaging, and the internal circuit of the network cable plug can be observed clearly by the X-ray image (Fig. 5e). To further estimate the spatial resolution of the $Pb_2CuGly_2Cl_4$ TFT array detector, the lead line pair card is utilized as the X-ray imaging target, and its maximum spatial resolution is up to 2.2 lp mm^{-1} in Fig. 5f. It should be noted that the spatial resolution is largely related to the pixel size of the TFT array, and further decreasing the pixel size can achieve a better spatial resolution.

4 Conclusions

In conclusion, we successfully synthesized high-quality 3D perovskitoid SCs $Pb_2CuGly_2X_4$ (Gly = -O_2C-CH_2-NH_2; X = Cl, Br) through amino acids ligands metal cross-linked strategy. The rigid $Cu(Gly)_2$ pillars and robust inorganic networks enabled by the face/edge-shared $[PbX_5O_3]^{9-}$ dodecahedron can synergistically inhibit the ion migration, leading to a high E_a of 1.06 eV. Compared with $Pb_2CuGly_2Br_4$, the $Pb_2CuGly_2Cl_4$ SC exhibits lower microstrain, lower defect density, higher E_a and higher resistivity. As a consequence, the fabricated $Pb_2CuGly_2Cl_4$ SC X-ray detector enables an excellent operating stability with a low dark current drift of 1.20×10^{-9} nA mm^{-1} s^{-1} V^{-1} under a high electric field (120 V mm^{-1}) and continuous X-ray irradiation. Besides, $Pb_2CuGly_2Cl_4$ SC detector also endows a high sensitivity of 9250 μC Gy^{-1} cm^{-2}. Furthermore, the $Pb_2CuGly_2Cl_4$ nanocrystals are dispersed in water, and the obtained $Pb_2CuGly_2Cl_4$ paste is blade-coated on TFT array to fabricate an X-ray imaging detector with a spatial resolution of 2.2 lp mm^{-1}. The amino acids ligands metal cross-linked strategy broadens the types of 3D perovskites with suppressed ion migration, and the facile preparation technique of integrated X-ray imaging detectors presents a promising prospect for practical applications in the future.

Acknowledgements This work is financially supported by the National Natural Science Foundation of China (62004089,

62374053, 62474187 and 12235006), the Special Zone Support Program for Outstanding Talents of Henan University, the Shenzhen Basic Research Program (JCYJ20220818101612027), the Guangdong Basic and Applied Basic Research Foundation (2024A1515012494), the Henan Province Postdoctoral Science Foundation (J23029Y), the Natural Science Foundation of Henan Province (232300420412), and the Science and Technology Tackling Project of Henan Province (242102210160).

Author Contributions Zimin Zhang and Xiaoli Wang contributed equally to this work; Huayang Li and Yanliang Liu conceived the idea, Huayang Li wrote the original manuscript, and Yanliang Liu and Shi Chen revised the manuscript; Huayang Li, Yanliang Liu and Shi Chen supervised the work; Zimin Zhang fabricated the perovskitoid SC and powder, carried out the structure analysis, did theoretical calculation and took the photoelectric property measurements. Xiaoli Wang, Dong Li and Yang Zhang fabricated the detectors based on SC and films, and performed the X-ray detection and X-ray imaging. All authors commented and reviewed the manuscript.

Declarations

Conflict of Interest The authors declare no interest conflict. They have no known competing financial interests or personal relationships that could have appeared to influence the work reported in this paper.

Supplementary Information The online version contains supplementary material available at https://doi.org/10.1007/s40820-025-01788-z.

References

1. X. He, Y. Deng, D. Ouyang, N. Zhang, J. Wang et al., Recent development of halide perovskite materials and devices for ionizing radiation detection. Chem. Rev. **123**(4), 1207–1261 (2023). https://doi.org/10.1021/acs.chemrev.2c00404
2. H. Wei, D. DeSantis, W. Wei, Y. Deng, D. Guo et al., Dopant compensation in alloyed $CH_3NH_3PbBr_{3-x}Cl_x$ perovskite single crystals for gamma-ray spectroscopy. Nat. Mater. **16**(8), 826–833 (2017). https://doi.org/10.1038/nmat4927
3. D. Chu, B. Jia, N. Liu, Y. Zhang, X. Li et al., Lattice engineering for stabilized black $FAPbI_3$ perovskite single crystals for high-resolution X-ray imaging at the lowest dose. Sci. Adv. **9**(35), 2255 (2023). https://doi.org/10.1126/sciadv.adh2255
4. Y. Liu, Y. Zhang, X. Zhu, J. Feng, I. Spanopoulos et al., Triple-cation and mixed-halide perovskite single crystal for high-performance X-ray imaging. Adv. Mater. **33**(8), e2006010 (2021). https://doi.org/10.1002/adma.202006010
5. J. Jiang, M. Xiong, K. Fan, C. Bao, D. Xin et al., Synergistic strain engineering of perovskite single crystals for highly stable and sensitive X-ray detectors with low-bias imaging and monitoring. Nat. Photonics **16**(8), 575–581 (2022). https://doi.org/10.1038/s41566-022-01024-9
6. Y. Liu, X. Zheng, Y. Fang, Y. Zhou, Z. Ni et al., Ligand assisted growth of perovskite single crystals with low defect density. Nat. Commun. **12**(1), 1686 (2021). https://doi.org/10.1038/s41467-021-21934-6
7. Y. Song, L. Li, M. Hao, W. Bi, A. Wang et al., Elimination of interfacial-electrochemical-reaction-induced polarization in perovskite single crystals for ultrasensitive and stable X-ray detector arrays. Adv. Mater. **33**(52), 2103078 (2021). https://doi.org/10.1002/adma.202103078
8. J. Peng, C.Q. Xia, Y. Xu, R. Li, L. Cui et al., Crystallization of $CsPbBr_3$ single crystals in water for X-ray detection. Nat. Commun. **12**(1), 1531 (2021). https://doi.org/10.1038/s41467-021-21805-0
9. X. Zhang, D. Chu, B. Jia, Z. Zhao, J. Pi et al., Heterointerface design of perovskite single crystals for high-performance X-ray imaging. Adv. Mater. **36**(3), 2305513 (2024). https://doi.org/10.1002/adma.202305513
10. D. Liu, Y. Zheng, X.Y. Sui, X.F. Wu, C. Zou et al., Universal growth of perovskite thin monocrystals from high solute flux for sensitive self-driven X-ray detection. Nat. Commun. **15**(1), 2390 (2024). https://doi.org/10.1038/s41467-024-46712-y
11. Y. Hua, G. Zhang, X. Sun, P. Zhang, Y. Hao et al., Suppressed ion migration for high-performance X-ray detectors based on atmosphere-controlled EFG-grown perovskite $CsPbBr_3$ single crystals. Nat. Photonics **18**(8), 870–877 (2024). https://doi.org/10.1038/s41566-024-01480-5
12. X. Xu, W. Qian, J. Wang, J. Yang, J. Chen et al., Sequential growth of 2D/3D double-layer perovskite films with superior X-ray detection performance. Adv. Sci. **8**(21), 2102730 (2021). https://doi.org/10.1002/advs.202102730
13. M. Girolami, F. Matteocci, S. Pettinato, V. Serpente, E. Bolli et al., Metal-halide perovskite submicrometer-thick films for ultra-stable self-powered direct X-ray detectors. Nano-Micro Lett. **16**(1), 182 (2024). https://doi.org/10.1007/s40820-024-01393-6
14. W. Wang, H. Meng, H. Qi, H. Xu, W. Du et al., Electronic-grade high-quality perovskite single crystals by a steady self-supply solution growth for high-performance X-ray detectors. Adv. Mater. **32**(33), 2001540 (2020). https://doi.org/10.1002/adma.202001540
15. F. Cui, P. Zhang, L. Zhang, Y. Hua, X. Sun et al., Liquid-phase epitaxial growth of large-area $MAPbBr_{3-n}Cl_n/CsPbBr_3$ perovskite single-crystal heterojunction for enhancing sensitivity and

stability of X-ray detector. Chem. Mater. **34**(21), 9601–9612 (2022). https://doi.org/10.1021/acs.chemmater.2c02266

16. Z. Xu, H. Xi, X. Sun, H. Liu, J. Liu et al., Highly stable and sensitive $(PEA)_2PbBr_4/CsPbBr_3$ single-crystal heterojunction X-R_ay detector with ultra-low detection limit. Adv. Funct. Mater. **34**(34), 2400817 (2024). https://doi.org/10.1002/adfm.202400817
17. C. Liu, Y. Yang, H. Chen, I. Spanopoulos, A.S.R. Bati et al., Two-dimensional perovskitoids enhance stability in perovskite solar cells. Nature **633**(8029), 359–364 (2024). https://doi.org/10.1038/s41586-024-07764-8
18. M. Xia, X. Sun, F. Ye, M. Liao, J. Liu et al., Stereo-hindrance engineering of a cation toward-oriented 2D perovskite with minimized tilting and high-performance X-ray detection. Adv. Mater. **36**(23), 2313663 (2024). https://doi.org/10.1002/adma.202313663
19. B. Zhang, T. Zheng, J. You, C. Ma, Y. Liu et al., Electron-phonon coupling suppression by enhanced lattice rigidity in 2D perovskite single crystals for high-performance X-ray detection. Adv. Mater. **35**(7), 2208875 (2023). https://doi.org/10.1002/adma.202208875
20. W. Li, X. Feng, K. Guo, W. Pan, M. Li et al., Prominent free charges tunneling through organic interlayer of 2D perovskites. Adv. Mater. **35**(18), e2211808 (2023). https://doi.org/10.1002/adma.202211808
21. M.E. Kamminga, H.-H. Fang, M.R. Filip, F. Giustino, J. Baas et al., Confinement effects in low-dimensional lead iodide perovskite hybrids. Chem. Mater. **28**(13), 4554–4562 (2016). https://doi.org/10.1021/acs.chemmater.6b00809
22. Y. Zhang, L. Zhu, Z. Yang, W. Tao, Z. Chen et al., Transient photoinduced Pb^{2+} disproportionation for exciton self-trapping and broadband emission in low-dimensional lead halide perovskites. J. Am. Chem. Soc. **146**(11), 7831–7838 (2024). https://doi.org/10.1021/jacs.4c01115
23. J.-J. Zhang, S.-Q. Xia, T.-L. Sheng, S.-M. Hu, G. Leibeling et al., A novel 2D net-like supramolecular polymer constructed from Ln_6Cu_{24} node and trans-$Cu(Gly)_2$ bridge. Chem. Commun. **10**, 1186–1187 (2004). https://doi.org/10.1039/b400447g
24. K. Guo, W. Li, Y. He, X. Feng, J. Song et al., Low bandgap 2D perovskite single crystal with anomalous-large charges/ions collection ratio for ultra-sensitive and stable X-ray detectors. Angew. Chem. Int. Ed. **62**(23), e202303445 (2023). https://doi.org/10.1002/anie.202303445
25. N. Mercier, A. Riou, An organic–inorganic hybrid perovskite containing copper paddle-wheel clusters linking perovskite layers: $[Cu(O_2C–(CH_2)_3–NH_3)_2]$ $PbBr_4$. Chem. Commun. (2004). https://doi.org/10.1039/B316847F
26. M.L. Aubrey, A. Saldivar Valdes, M.R. Filip, B.A. Connor, K.P. Lindquist et al., Directed assembly of layered perovskite heterostructures as single crystals. Nature **597**(7876), 355–359 (2021). https://doi.org/10.1038/s41586-021-03810-x
27. W. Bi, N. Mercier, N. Louvain, M. Latroche, Lead halide layers linked by trans-$Cu(gly)_2$ (gly =$–O_2C–CH_2–NH_2$) pillars in heterometallic glycinate based organic–inorganic hybrids. Eur. J. Inorg. Chem. **2006**(21), 4225–4228 (2006). https://doi.org/10.1002/ejic.200600634
28. S. Gómez-Salces, F. Aguado, R. Valiente, F. Rodríguez, Unraveling the coordination geometry of copper(II) ions in aqueous solution through absorption intensity. Angew. Chem. Int. Ed. **51**(37), 9335–9338 (2012). https://doi.org/10.1002/anie.201202033
29. K. Parashar, Z. Zhang, V. Buturlim, J. Jiang, A. Roseborough et al., Structural and physical properties of two distinct 2D lead halides with intercalated Cu(II). J. Mater. Chem. C **12**(25), 9372–9384 (2024). https://doi.org/10.1039/D4TC01322K
30. W. Pan, Y. He, W. Li, L. Liu, K. Guo et al., Cation-π interactions enabled water-stable perovskite X-ray flat mini-panel imager. Nat. Commun. **15**(1), 257 (2024). https://doi.org/10.1038/s41467-023-44644-7
31. M. Han, Y. Xiao, C. Zhou, Z. Xiao, W. Tan et al., Suppression of ionic and electronic conductivity by multilayer heterojunctions passivation toward sensitive and stable perovskite X-ray detectors. Adv. Funct. Mater. **33**(35), 2303376 (2023). https://doi.org/10.1002/adfm.202303376
32. Y. Zhang, Y. Liu, S. Liu, Composition engineering of perovskite single crystals for high-performance optoelectronics. Adv. Funct. Mater. **33**(9), 2210335 (2023). https://doi.org/10.1002/adfm.202210335
33. H. Li, J. Song, W. Pan, D. Xu, W.-A. Zhu et al., Sensitive and stable 2D perovskite single-crystal X-ray detectors enabled by a supramolecular anchor. Adv. Mater. **32**(40), 2003790 (2020). https://doi.org/10.1002/adma.202003790
34. Y. Huang, L. Qiao, Y. Jiang, T. He, R. Long et al., A-site cation engineering for highly efficient $MAPbI_3$ single-crystal X-ray detector. Angew. Chem. Int. Ed. **58**(49), 17834–17842 (2019). https://doi.org/10.1002/anie.201911281
35. D. Pariari, S. Mehta, S. Mandal, A. Mahata, T. Pramanik et al., Realizing the lowest bandgap and exciton binding energy in a two-dimensional lead halide system. J. Am. Chem. Soc. **145**(29), 15896–15905 (2023). https://doi.org/10.1021/jacs.3c03300
36. M. Xia, J.-H. Yuan, G. Niu, X. Du, L. Yin et al., Unveiling the structural descriptor of $A_3B_2X_9$ perovskite derivatives toward X-ray detectors with low detection limit and high stability. Adv. Funct. Mater. **30**(24), 1910648 (2020). https://doi.org/10.1002/adfm.201910648
37. Z. Zhao, J. Hao, B. Jia, D. Chu, J. Pi et al., Epitaxial welding of 3D and 2D perovskite single crystals for direct-indirect energy-conversion X-ray detection and imaging. ACS Energy Lett. **9**(6), 2758–2766 (2024). https://doi.org/10.1021/acsenergylett.4c00590
38. S. Dong, Z. Fan, W. Wei, S. Tie, R. Yuan et al., Bottom-up construction of low-dimensional perovskite thick films for high-performance X-ray detection and imaging. Light Sci. Appl. **13**(1), 174 (2024). https://doi.org/10.1038/s41377-024-01521-2